Zwitterionic sulfhydryl sulfobetaine stabilized platinum nanoparticles for enhanced dopamine detection and anti-tumor ability

Ruyu Li[1], Liyuan Fan[1], Shengfu Chen[2], Longgang Wang[1], Yanshuai Cui[3], Guanglong Ma[4], Xiaoyu Zhang[1], Zhiwei Liu[1]*

[1]State Key Laboratory of Metastable Materials Science and Technology, Hebei Key Laboratory of Nano-biotechnology, Hebei Key Laboratory of Applied Chemistry, Yanshan University, Qinhuangdao, 066004, China

[2]Key Laboratory of Biomass Chemical Engineering of Ministry of Education, College of Chemical and Biological Engineering, Zhejiang University, Hangzhou, Zhejiang 310027, China

[3]Hebei University of Environmental Engineering, Qinhuangdao, 066102, China

[4]Centre for Cancer Immunology, Faculty of Medicine, University of Southampton, Southampton, SO166YD, UK

ABSTRACT

Herein, three kinds of molecules were used to modify the surface of platinum nanoparticles (Pt NPs) to tune their surface charge. Zwitterionic thiol-functionalized sulfobetaine (SH-SB) stabilized Pt NPs (SH-SB/Pt NPs) had the highest oxidase activity and peroxidase activity in prepared platinum nanozyme due to the generation of reactive oxygen species. In addition, a colorimetric dopamine detection method was established based on the peroxidase activity of SH-SB/Pt NPs. This method had wide range (0-120 μM), low detection limit (0.244 μM), and high specificity. More importantly, SH-SB/Pt NPs displayed little hemolysis and good stability in the presence of proteins. SH-SB/Pt NPs demonstrated high cytotoxicity *in vitro* and good anti-tumor ability *in vivo*, which was attributed to the photothermal conversion ability of SH-SB/Pt NPs and generation of reactive oxygen species in acidic environment. The surface modification of nanozymes using zwitterionic molecules opens a new method to improve the catalytic activity and anti-tumor ability of nanozyme.

KEYWORDS: zwitterionic; nanozyme; detection; dopamine; anti-tumor

1. INTRODUCTION

Dopamine (DA) exists in various organs and fluids in humans and animals.[1] It is an important catecholamine neurotransmitter and plays an important role in the nervous system. The imbalance of DA content can lead to a variety of diseases, such as Alzheimer's disease, Parkinson's disease, schizophrenia, and involuntary shaking of hands and feet.[2, 3] Therefore, it is urgent to find a simple and accurate method with high sensitivity to detect the content of DA in the human body. The colorimetric method is a simple, fast and sensitive analytical

detection method.[4,5] In addition, it is urgent to develop new drugs to treat the cancer which has resulted in serious health problems. Natural enzymes which have high substrate specificity and efficiency in biological solution, such as horseradish peroxidase (HRP), glucose oxidase (GOD) and oxidase have been used as biocatalysts in colorimetric analysis and anti-tumor therapy.[6,7] However, the sensitivity to environmental changes and difficulty in extraction and separation limit their storage and use.[8] Therefore, it is necessary to develop nanozymes to maintain the catalytic activity of natural enzymes and overcome their shortcomings.

Since the discovery of the inorganic Fe_3O_4 nanoparticles which mimic the function of peroxidase in 2007,[9] many nanozymes such as metal nanoparticles,[10,11] pyrite,[12] carbon,[13] single-atom catalysts,[14] and MoS_2[15] have been developed to mimic the function of natural enzymes in recent years. Nanozymes have the advantage of easy preparation and storage, high specific surface area, and djustable activity.[16,17] The natural enzymes play important function in bio-related medium, nanozymes should function in the same environment. The catalytic ability and stability in biological solution are closely related with their surface properties.[18,19] Therefore, it is necessary to study the effect of surface properties on the catalytic activity of nanozymes. Though many nanozymes have been successfully prepared, there was few research on the effect of surface charge on the catalytic activity of nanozymes.

In recent years, noble metal nanoparticles have attracted great attentions due to their applications in biological sensors and as anti-tumor agents.[20-22] The detection performance of noble metal nanoparticles depends on their catalytic activity in bio-related medium. To

enhance their catalytic activity, doping with metals is a commonly used method to prepare highly active nanoalloys. However, high-quality and stable nanoalloys are difficult to synthesize. Ligand modification is another useful strategy for improving the catalytic activity by changing the surface chemistry.[23,24] Jiang et al found that amine-rich ligand improves the catalytic activity of gold nanoparticles compared with other ligands and unmodified AuNPs.[23] Gao et al reported the peroxidase and catalase-like activities of gold, silver, platinum and palladium are pH-switchable.[25] In addition, chemodynamic therapy (CDT) has been explored to obtain anti-tumor efficacy of nanozymes. The nanozymes can kill cancer cells by interacting with endogenous O_2 or H_2O_2 to produce reactive oxygen species (ROS) that promotes cell apoptosis.[26,27] The noble metal nanozymes also have been widely used in photothermal therapy (PTT) under near-infrared (NIR) light, which has the advantages of non-invasive, low toxicity, and simple operation.[28] The performance of photothermal reagents depends on their photothermal conversion properties and stability in fibrinogen solution. But the poor stability reduced their photothermal conversion efficacy. The surface modification with organic molecules will improve their stability and photothermal conversion efficacy. Thus, adjusting surface charge should be a useful method to tune the catalytic activity and stability. And zwitterionic molecules may be good for addressing both problems due to their biocompatibility and electric conduction ability.

Platinum nanoparticles have good catalytic activity and photothermal conversion ability among noble metal nanoparticles. In this work, three kinds of organic ligands thiol-

functionalized sulfobetaine (SH-SB), β-cysteamine (β-MEA), and mercaptopropionic acid (3-MPA) were used to modify Pt nanoparticles to prepare SH-SB/Pt NPs, β-MEA/Pt NPs and 3-MPA/Pt NPs, and the zeta potentials of the modified nanoparticles were neutral, positive and negative, respectively. The zeta potential greatly affected the hydrodynamic size, stability and catalytic activity of modified Pt NPs. SH-SB/Pt NPs with the zwitterionic surface and cubic Pt NPs had the highest catalytic activity. SH-SB/Pt NPs were also water-soluble and stable in protein solution. Based on the good peroxidase activity of SH-SB/Pt NPs, SH-SB/Pt NPs were used to establish a colorimetric method to detect the DA content and recovery rate in actual samples. The detection of DA was sensitive, selective and convenient. In addition, SH-SB/Pt NPs were used for CDT/PTT co-therapy of tumors based on their high enzyme activity and photothermal properties. MTT assay was used to study the toxicity of SH-SB/Pt NPs on HeLa and A549 cells *in vitro*, the viability of HeLa and A549 cells was 10% when they were treated with SH-SB/Pt NPs+NIR at 200 μg/mL. The final tumor inhibition rate of SH-SB/Pt NPs+NIR group was 96.48% *in vivo*. These results indicated that SH-SB/Pt NPs were promising nanomaterials for DA diagnosis and anti-tumor applications.

2. MATERIALS AND METHODS

2.1 Materials and apparatus

Potassium tetrachloroplatinate (K_2PtCl_4), H_2O_2 (30%), 3,3',5,5'-tetramethylbenzidine (TMB), dopamine (DA), o-phenylenediamine (OPD), and thiazole blue (MTT) were purchased from Aladdin. β-cysteamine (β-MEA), 3-mercaptopropionic acid (3-MPA) and sodium borohydride ($NaBH_4$) were purchased from Saen Chemical Technology Co., Ltd. 2, 2'-azino-bis (3-

ethylbenzothiazoline-6-sulfonic acid) (ABTS) was purchased from BOMEI. Dialysis bags (MWCO=8000-14,000) were purchased from Spectrum Laboratories Inc. The thiol-functionalized sulfobetaine (SH-SB) was synthesized by our laboratory according to previous report.[29] HeLa cells and A549 cells were purchased from Center for Typical Culture Collection.

UV-Vis spectra were obtained using a TU1810 spectrophotometer. The particle size and morphology of the nanoparticles were characterized by TEM (HT 7700). A 10 μL pipette was used to drop SH-SB/Pt NPs solution onto a copper net covered with carbon film, and the sample morphology was observed by HT 7700 after air drying. The infrared peak was measured by an infrared spectrometer (E55-FRA106). The X-ray diffraction peaks were obtained by an X-ray diffractometer (Kratos AXIS Ultra). The hydrodynamic size and zeta potential were determined by Zetasizer Nano-ZS90. To explore the stability of SH-SB/Pt NPs in protein solution, the hydrodynamic size of mixed solution of fibrinogen and SH-SB/Pt NPs after incubation for 24 h was tested at pH 7.4.

2.2 Synthesis of nanozyme

2 mL K_2PtCl_4 solution (0.83 mg/mL) was added into a 5 mL round bottom flask, and 300 μL $NaBH_4$ solution (1.51 mg/mL) was added to reduce the K_2PtCl_4 solution. Then 19.37 μL SH-SB solution (5.00 mg/mL), β-MEA solution (43.43 mg/mL) and 3-MPA solution (261.23 mg/mL) were added to the mixture, respectively, as shown in **Scheme 1**. The above mixtures were bubbled with N_2 at 30℃ for 30 min, and incubated for 3 h. The solutions were dialyzed against water to obtain SH-SB modified Pt NPs (SH-SB/Pt NPs), β-MEA modified Pt NPs (β-MEA/Pt NPs) and 3-MPA modified Pt NPs (3-MPA/Pt NPs), respectively.

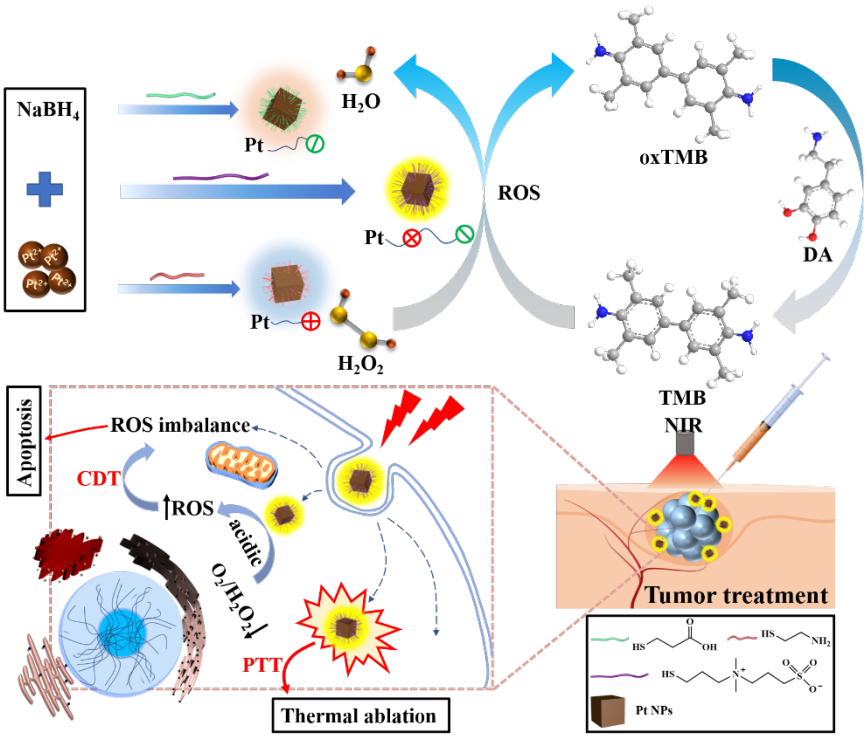

Scheme 1. Synthesis of 3-MPA/Pt NPs, SH-SB/Pt NPs and β-MEA/Pt NPs for enhanced dopamine detection and anti-tumor ability

2.3 Enzyme activity

The oxidase activities of SH-SB/Pt NPs, β-MEA/Pt NPs and 3-MPA/Pt NPs were measured and compared by catalysis of TMB. 900 μL TMB solution (0.6 mM, pH 4) and 370 μL HAc-NaAc solution were incubated at 30°C for 5 min, and then 50 μL SH-SB/Pt NPs, β-MEA/Pt NPs and 3-MPA/Pt NPs solution (C_{Pt}=1.725 mM) were added separately and continued to incubate for 2 min. Finally, the UV-Vis spectra of mixed solution were measured to determine the oxidase activity of the three kinds of nanoparticles.

The peroxidase activities of the three kinds of nanoparticles were also compared. 900 μL TMB solution (0.6 mM, pH 4) and 370 μL HAc-NaAc solution (pH 4) were incubated at 30°C

for 5 min, and 50 μL SH-SB/Pt NPs, β-MEA/Pt NPs and 3-MPA/Pt NPs solution (C_{Pt}=1.725 mM) were added separately and continued to incubate for 5 min. Then 50 μL H_2O_2 solution (0.1 M) was added and incubated for 2 min. Finally, it was judged whether the three kinds of nanoparticles had peroxidase activity by observing the UV-Vis spectra of mixed solution.

2.4 Determination of catalytic mechanism

The catalytic mechanism of oxidase activity of SH-SB /Pt NPs was tested. P-benzoquinone (BQ),[30] NaN_3,[31] IPA[32] and EDTA[33] was used as scavengers to superoxide anions ($O_2^{\cdot-}$), singlet oxygen ($^1O_2$), hydroxyl radicals (·OH), and hole (h^+), respectively. As for [TMB+ SH-SB /Pt NPs] group, 900 μL TMB (0.6 mM) solution, 50 μL SH-SB/Pt NPs (C_{Pt} =1.725 mM) and HAc-NaAc solution were mixed. BQ (100 μL, 10 mM), NaN_3 (100 μL, 30 mM), IPA (100 μL, 4 M), and EDTA (100 μL, 50 mM) were added, respectively. The absorbance was measured by UV-Vis spectrophotometer.

The catalytic mechanism of peroxidase activity of SH-SB/Pt NPs was also tested. As for [TMB+H_2O_2+SH-SB/Pt NPs] group, 900 μL TMB (0.6 mM) solution, 30 μL SH-SB/Pt NPs (C_{Pt} =1.725 mM), 30 μL H_2O_2 (50 mM) and HAc-NaAc solution were mixed. The absorbance was measured by UV-Vis spectrophotometer. Then, (i) 200 μL IPA (5 M), (ii) 200 μL BQ (2 mM), 200 μL NaN_3 (1 mM), (iii) 200 μL IPA (5 M), 200 μL BQ (10 mM), 200 μL NaN_3 (10 mM) and [TMB+H_2O_2+SH-SB/Pt NPs] group were incubated for 5 min, 15 min, 10 min, respectively. The absorbance was measured by UV-Vis spectrophotometer.

2.5 Optimization of catalytic conditions

To find the optimal pH, we prepared HAc-NaAc buffer solution of different pH, and then used HAc-NaAc buffer solution of different pH to dissolve TMB powder to obtain TMB solution of different pH. 900 μL TMB solution and 370 μL HAc-NaAc solution of different pH were added and incubated at 30℃ for 5 min, then 50 μL SH-SB/Pt NPs solution (C_{Pt}=1.725 mM) was added and incubated for 5 min, and 50 μL H_2O_2 solution (0.1 M) was added and incubated for 5 min. Finally, the absorbance at 652 nm of the mixed solution (pH 1-12) was obtained, and the optimal pH of the peroxidase activity of SH-SB/Pt NPs was obtained by analyzing the obtained absorbance.

In addition, the optimum temperature of SH-SB/Pt NPs was also explored. 900 μL TMB solution (0.6 mM, pH 4) and 370 μL HAc-NaAc solution (pH 4) were added, and the mixture was incubated at different temperatures (20-80℃) for 5 min. Then 50 μL SH-SB/Pt NPs solution (C_{Pt}=1.725 mM) was added and incubated for 5 min, and 50 μL H_2O_2 solution (0.1 M) was added and incubated for 5 min. Finally, the absorbance at 652 nm of the mixed solution at 20-80℃ were obtained, and the optimal temperature of the peroxidase activity of SH-SB/Pt NPs was obtained by analyzing the obtained absorbance.

2.6 Determination of kinetic parameters

Firstly, the effect of different concentrations of TMB on catalytic kinetics was examined. 30 μL SH-SB/Pt NPs (C_{Pt} =1.725 mM), 50 μL H_2O_2 (50 mM) and HAc-NaAc solution (0.2 M, pH 4) were mixed and incubated at 30℃ for 5 min. Different concentrations of TMB solutions

(0.05-0.51 mM) were mixed with the above solutions, The absorbance at 652 nm of solution was measured. Then the influence of different concentrations of H_2O_2 on catalytic kinetics was tested. 900 μL TMB (0.6 mM) and 370 μL HAc-NaAc solution (0.2 M, pH 4) were mixed and incubated at 30℃ for 5 min. Then, 30 μL SH-SB/Pt NPs (C_{Pt} =1.725 mM) and different concentrations of H_2O_2 (0.19-7.69 mM) were mixed with the above solutions, respectively. Finally, the absorbance at 652 nm of solution was measured.

2.7 Establishment of DA detection platform

550 μL different concentrations of DA solution (0-220 μM), 30 μL SH-SB/Pt NPs (C_{Pt} =1.725 mM), 30 μL H_2O_2 (150 mM) and 100 μL HAc-NaAc solution (0.2 M, pH 4) were mixed and incubated at 30℃ for 5 min. Then, 900 μL TMB solution (0.6 mM) was added for further incubation for 5 min. Finally, the absorbance at 652 nm was measured. Finally, the selectivity of this method was measured.

2.8 Experiment *in vitro*

In order to explore the photothermal properties of SH-SB/Pt NPs to treat tumor cells, HeLa cells and A549 cells were treated by 200 μL of SH-SB/Pt NPs solution (12.5- 100 μg/mL), SH-SB solution (100 μg/mL), Pt NPs solution (100 μg/mL) and DMEM, respectively. After 4 h, each well was irradiated for 10 min. Cell viability of cells with samples after photothermal irradiation was obtained according to previous report.[34] In addition, 200 μL of SH-SB/Pt NPs solution (12.5- 100 μg/mL) at pH 7.4 and pH 5.5 was added to treat HeLa and A549 cells to study the effect of CDT of SH-SB/Pt NPs.

2.9 Anti-tumor experiment *in vivo*

All experiments involving animals were performed in accordance with the statute of Experimental Animal Ethics Committee of Yanshan University. The groups of female KM mice were set: Ⅰ: Saline; Ⅱ: Saline + NIR; Ⅲ: Pt NPs; Ⅳ: SH-SB/Pt NPs; Ⅴ: SH-SB/Pt NPs+NIR (n=6). U14 cells were injected to create tumor-bearing mouse models. When the tumor grew to about 100 mm^3, the mice were given the drug (3 mg/kg). During this period, 50 μL sample was injected every two days and irradiated for 10 min. After 14 days, the main organs and body indexes of mice were obtained. The concentration of alanine aminotransferase (ALT) and aspartate aminotransferase (AST) in the blood was also tested. The tumor volume and tumor inhibition rate were calculated using formula1 and 2.

$$V = \frac{a \times b^2}{2} \quad (1)$$

$$\text{Tumor inhibition rate (TIR, \%)} = \frac{V_{\text{control}} - V_{\text{experiment}}}{V_{\text{control}}} \times 100 \quad (2)$$

V means the tumor volume, a is the long diameter of tumor, b is the short diameter of tumor.

3. RESULTS AND DISCUSSION

3.1 Structure of SH-SB/Pt NPs, β-MEA/Pt NPs, 3-MPA/Pt NPs

SH-SB/Pt NPs, β-MEA/Pt NPs and 3-MPA/Pt NPs were successfully synthesized, and SH-SB/Pt NPs had the best stability as shown in **Figure S1**. The EDX, XPS, SEM mapping and FTIR of SH-SB/Pt NPs also proved that SH-SB/Pt NPs were synthesized successfully in **Figure S2** and **Figure S3**. The cube-shaped of Pt NPs, SH-SB/Pt NPs, β-MEA/Pt NPs and 3-MPA/Pt NPs

were synthesized as shown in **Figure 1a, b, c** and **d**. The size of Pt NPs was 7.71±0.72 nm, and the dispersion was very poor. On the contrary, the SH-SB/Pt NPs with regular cubes had good dispersibility, and the size was 6.97+1.44 nm. The sizes of β-MEA/Pt NPs and 3-MPA/Pt NPs were 7.04±0.47 nm and 14.64±0.99 nm, respectively. And there were almost no monodisperse nanoparticles of β-MEA/Pt NPs and 3-MPA/Pt NPs. Thus, the dispersion of the SH-SB/Pt NPs was better than that of Pt NPs, β-MEA/Pt NPs and 3-MPA/ Pt NPs.

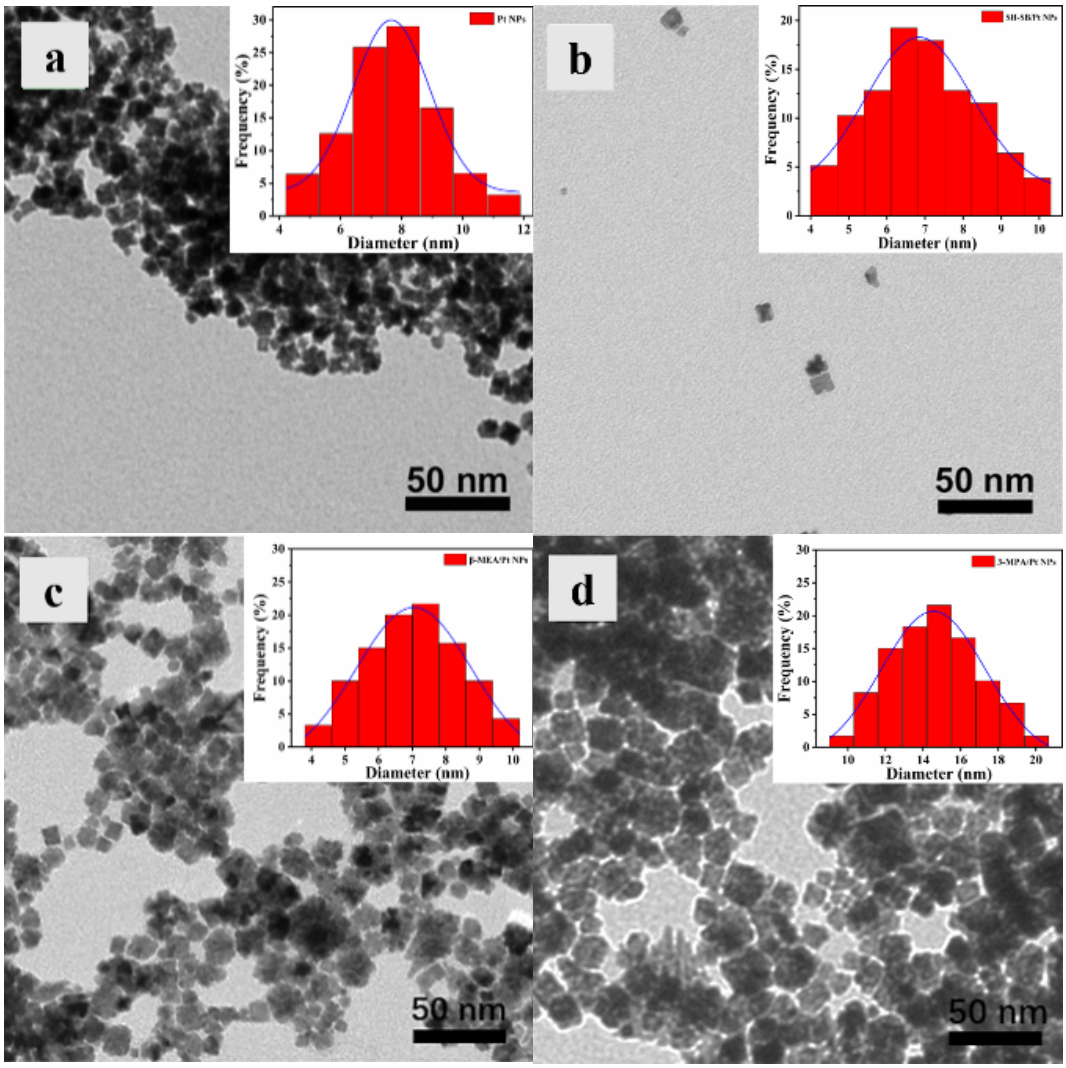

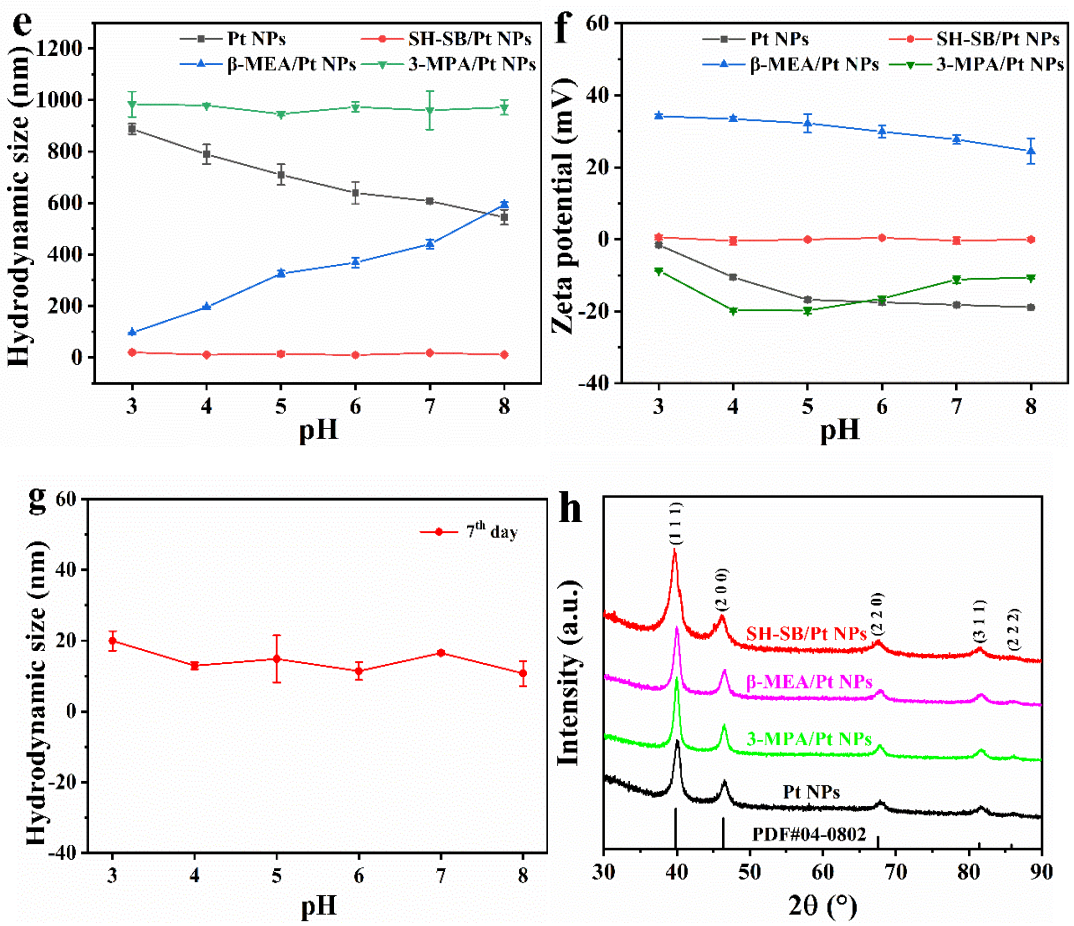

Figure 1. TEM images of (a) Pt NPs, (b) SH-SB/Pt NPs, (c) β-MEA/Pt NPs and (d) 3-MPA/ Pt NPs; (e) Hydrodynamic size and (f) zeta potential of Pt NPs, SH-SB/Pt NPs, β-MEA/Pt NPs and 3-MPA/Pt NPs; (g) hydrodynamic size on 7th day of SH-SB/Pt NPs and (h) XRD of SH-SB/Pt NPs, β-MEA/Pt NPs, 3-MPA/Pt NPs and Pt NPs

The hydrodynamic size and zeta potential of Pt NPs, SH-SB/Pt NPs, β-MEA/Pt NPs and 3-MPA/Pt NP were measured at pH 3-8. As shown in **Figure 1e** and **f**, the hydrodynamic size of the Pt NPs decreased from 900 nm to 500 nm, and the zeta potential increased from 0 to -20 mV at pH 3-8. The hydrodynamic size of β-MEA/Pt NPs increased from 100 nm to 600 nm, and the zeta potential decreased from 35 mV to 25 mV. The hydrodynamic size of 3-MPA/Pt

NPs was about 900 nm, and the zeta potential was negative. Pt NPs, β-MEA/Pt NPs and 3-MPA/Pt NPs were obviously precipitated after several hours. β-MEA and 3-MPA did not effectively stabilize Pt nanoparticles. In contrast, the hydrodynamic size of SH-SB/Pt NPs was between 10 and 20 nm when SH-SB/Pt NPs were under the same conditions, which proved that SH-SB/Pt NPs were stable under different pH. It should be noted that the hydrodynamic size of Pt nanoparticles measured by DLS was larger than that of Pt nanoparticles measured by TEM. In addition, the zeta potential of SH-SB/Pt NPs was about 0 mV, which was consistent with the characteristics of zwitterionic group. Therefore, we synthesized three kinds of Pt-based nanoparticles with different surface charges using SH-SB, β-MEA and 3-MPA.

Compared with the unstable β-MEA/Pt NPs and 3-MPA/Pt NPs, the hydrodynamic size of SH-SB/Pt NPs varied between 10.76 and 19.96 nm after 7 d in **Figure 1g**, which proved that the Pt NPs modified with zwitterionic SH-SB were stable. The XRD patterns of Pt NPs, SH-SB/Pt NPs, β-MEA/Pt NPs and 3-MEA/Pt NPs were obtained to further explore their structure in **Figure 1h**. The results strongly proved the successful synthesis of the several cubic Pt-based nanoparticles without changing the face-centered cubic structure of Pt NPs. Thus, the addition of various ligands did not affect their crystal form, which laid a solid foundation for the subsequent research on the effect of zeta potential on catalytic activity.

3.2. Enzyme activity

The oxidase-like activity of Pt NPs, SH-SB/Pt NPs, β-MEA/Pt NPs and 3-MPA/Pt NPs was tested. As shown in **Figure 2a**, compared with Pt NPs, β-MEA/Pt NPs and 3-MPA/Pt NPs, the

absorbance of [SH-SB/Pt NPs+TMB] at 652 nm was the highest (0.416), which was more than 9 times that of Pt NPs (0.045), β-MEA/Pt NPs (0.026) and 3-MPA/Pt NPs (0.024), indicating that SH-SB/Pt NPs oxidized the most of TMB to oxTMB. In addition, the similar results were obtained in the catalyzed reaction of OPD and ABTS. Therefore, the oxidase activity of SH-SB/Pt NPs far exceeded that of Pt NPs, β-MEA/Pt NPs and 3-MPA/Pt NPs. In addition, the peroxidase-like activity of Pt NPs, SH-SB/Pt NPs, β-MEA/Pt NPs and 3-MPA/Pt NPs was tested. After adding H_2O_2, the absorbance of SH-SB/Pt NPs at 652 nm was 1.336, which was 2.32 times than that of Pt NPs. What's more, the absorbance of SH-SB/Pt NPs (1.336) was more 10 times than that of β-MEA/Pt NPs and 3-MPA/Pt NPs in **Figure 2b**. And similar results were obtained in the catalyzed reaction of OPD and ABTS as shown in **Figure 2c, d, e** and **f**. Therefore, SH-SB/Pt NPs had the strongest enzyme activity among the four types of nanoparticles.

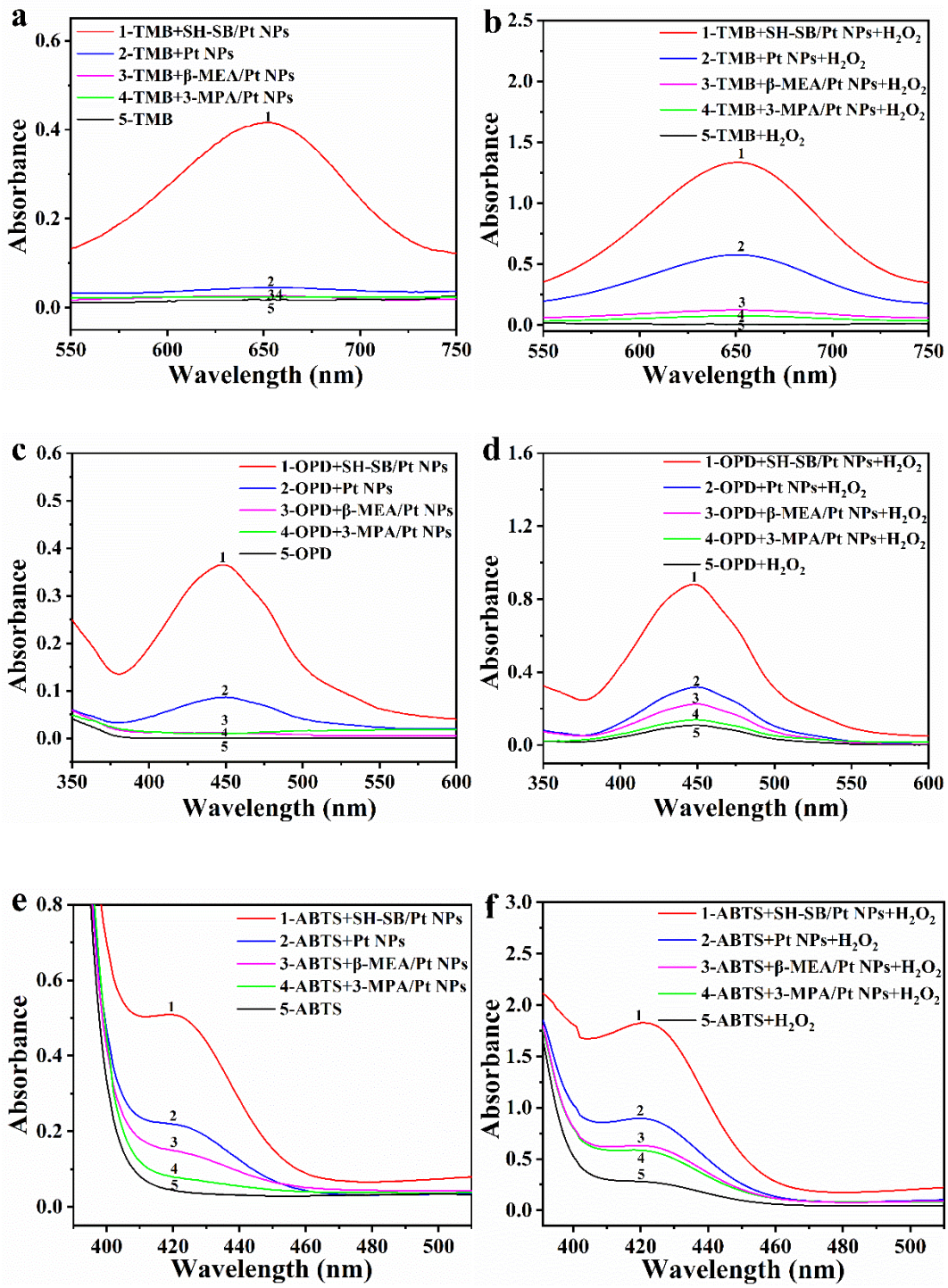

Figure 2. Oxidase activity of different substrates: (a) TMB; (c) OPD; (e) ABTS; Peroxidase activity of different substrates: (b) TMB; (d) OPD; (f) ABTS

The significant difference of enzyme activity should be due to the different physicochemical properties of Pt NPs, SH-SB/Pt NPs, β-MEA/Pt NPs and 3-MPA/Pt NPs. The morphology difference of these samples was not obvious enough in TEM images. But they had different hydrodynamic size and zeta potential in HAc-NaAc solution. Among them, SH-SB/Pt NPs had the smallest hydrodynamic size and excellent stability because of zwitterionic SH-SB. When the experiment was carried out at pH 4, the zeta potential of SH-SB/Pt NPs, β-MEA/Pt NPs, 3-MPA/Pt NPs was -0.44±1.20, 33.40±0.65, -19.70±0.49 mV, and the hydrodynamic size of SH-SB/Pt NPs, β-MEA/Pt NPs, 3-MPA/Pt NPs was 10.44±2.50, 195.30±2.43, 979.05±1.27 nm, respectively. Zwitterionic ligand SH-SB was beneficial to the enhancement of the catalytic activity of the Pt-based nanoparticles compared with positively charged ligand β-MEA and negatively charged ligand 3-MPA.

3.3 Catalytic mechanism

In order to study the oxidase catalysis mechanism of SH-SB/Pt NPs, TMB was used as the chromogenic substrate. The catalytic oxidation of TMB may be related to ROS, including $^1O_2$, $O_2^{\cdot-}$, oxygen vacancy and ·OH. Therefore, the catalytic mechanism of SH-SB/Pt NPs was further studied. NaN_3 was added as a scavenger of $^1O_2$. As shown in **Figure 3a**, the group [TMB +SH-SB/Pt NPs] produced an obvious absorption peak at 652 nm with an absorbance value of about 0.7 after mixed incubation for 10 min. The absorbance at 652 nm of group [TMB+ SH-SB/Pt NPs +NaN_3] was 0.2. In addition, p-benzoquinone (BQ) was used as $O_2^{\cdot-}$ scavenging agent. As shown in **Figure 3b**, the group [TMB+ SH-SB/Pt NPs +BQ] also produced much lower

absorbance at 652 nm than group [TMB +SH-SB/Pt NPs]. Thus, NaN_3 and BQ inhibited the oxidase activity of SH-SB/Pt NPs, and $^1O_2$ and $O_2^{\cdot-}$ were ROS in the system, which were influencing factors of group [TMB+ SH-SB/Pt NPs]. Meanwhile, EDTA and isopropanol (IPA) are scavengers of oxygen vacancy and ·OH, respectively. As shown in **Figure 3c** and **d**, the absorbance of [TMB+SH-SB/Pt NPs+EDTA] and [TMB+SH-SB/Pt NPs+IPA] was not obviously different from [TMB+SH-SB/Pt NPs]. These results indicated that the oxidase activity of SH-SB/Pt NPs was not affected by oxygen vacancy and ·OH. In short, SH-SB/Pt NPs oxidized TMB by producing $^1O_2$ and $O_2^{\cdot-}$.

As shown in **Figure 3e**, BQ and NaN_3 were added in group [TMB+H_2O_2+ SH-SB/Pt NPs] for co-incubation for 15 min. Compared with group [TMB+H_2O_2+SH-SB/Pt NPs] at 652 nm (0.620), the absorbance of group [TMB+H_2O_2+SH-SB/Pt NPs+BQ+NaN_3] was 0.327, which indicated that BQ+NaN_3 inhibited the peroxidase activity of SH-SB/Pt NPs. $O_2^{\cdot-}$ and $^1O_2$ were generated in the catalytic process. As shown in **Figure 3f**, IPA was added and incubated for 5 min, group [TMB+H_2O_2+SH-SB/Pt NPs+IPA] and group [TMB+SH-SB/Pt NPs] had relatively close absorbance at 652 nm. The results showed that IPA inhibited the peroxidase activity of SH-SB/Pt NPs. At the same time, when BQ, NaN_3 and IPA were added to group [TMB+H_2O_2+SH-SB/Pt NPs] in **Figure 3g**, the absorbance at 652 nm of group [TMB+H_2O_2+SH-SB/Pt NPs+BQ+NaN_3+IPA] disappeared. Through the combined action of BQ, NaN_3 and IPA, the peroxidase activity of SH-SB/Pt NPs was completely inhibited. As shown in **Figure 3h**, the catalytic kinetic formula $v=\Delta A/\Delta b\Delta t$ was used to calculate the initial reaction rate at the same

time (Δt=24 s), v_1=2.40×10^{-8} Ms^{-1}, v_2=1.38×10^{-8} Ms^{-1}. The results proved that the catalytic activity of SH-SB/Pt NPs was enhanced after addition of H_2O_2, which should be due to more ROS was produced. To sum up, the peroxidase activity of SH-SB/Pt NPs was affected by $O_2^{\cdot-}$, $^1O_2$ and ·OH.

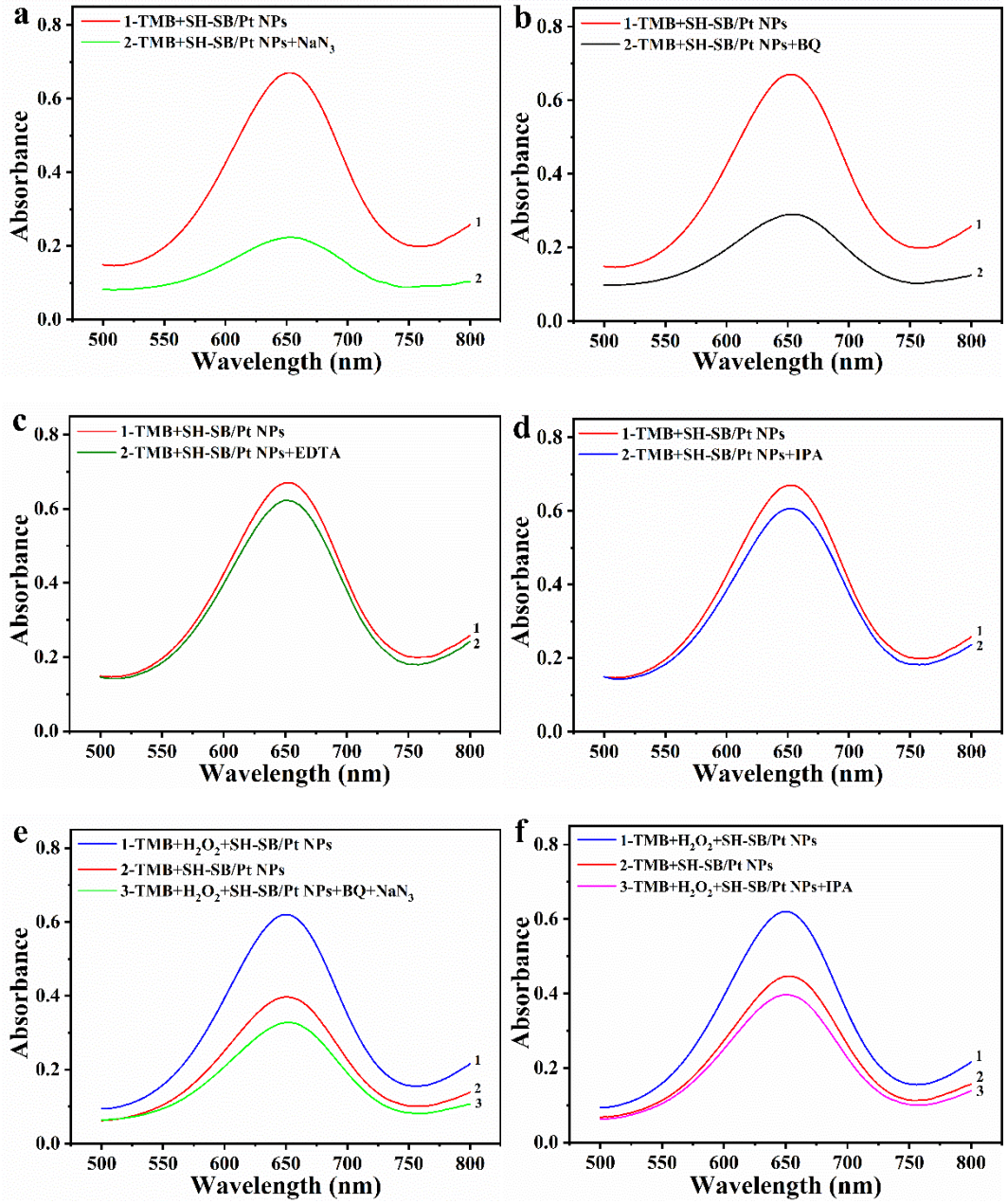

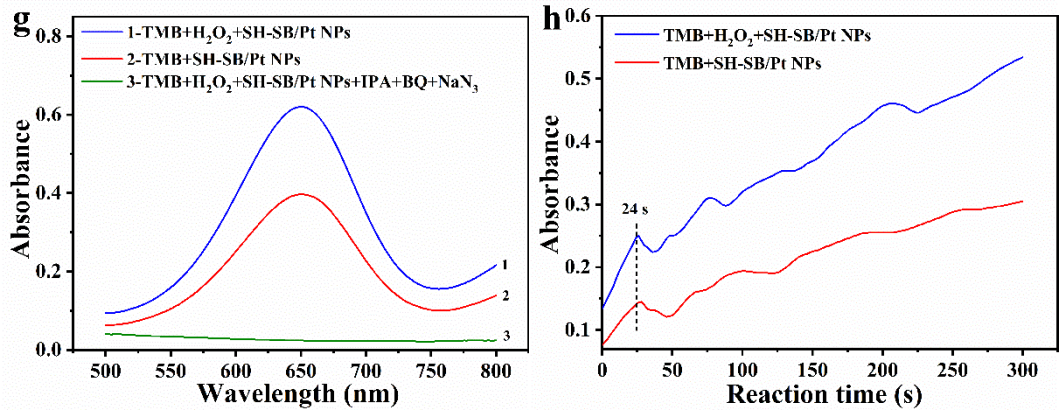

Figure 3. Study on the mechanism of oxidation activity: (a) NaN_3 (30 mM); (b) BQ (10 mM); (c) EDTA (50 mM); (d) IPA (4 M) and study on the mechanism of peroxidase activity: (e) BQ (2 mM)+NaN_3 (1 mM); (f) IPA (5 M); (g) IPA+BQ+NaN_3; (h) Time scan of [TMB+H_2O_2+SH-SB/Pt NPs] and [TMB+SH-SB/Pt NPs]

3.4 Optimization of peroxidase activity and stability

The influence of temperature and pH on the peroxidase activity of SH-SB/Pt NPs was explored. The absorbance of the mixed solution of [TMB+SH-SB/Pt NPs+ H_2O_2] at 652 nm was measured under different temperature and pH. As shown in **Figure 4a**, SH-SB/Pt NPs lost most of catalytic activity in strong acidic and alkaline environments. When the pH of solution increased from 1 to 4, the catalytic activity of SH-SB/Pt NPs gradually increased, and when pH=4, the relative activity of SH-SB/Pt NPs was the highest. When pH > 4, the catalytic activity of SH-SB/Pt NPs decreased sharply. The relative activity of SH-SB/Pt NPs was less than 10% when the pH≥ 5. Therefore, SH-SB/Pt NPs showed the highest catalytic activity at pH 4. In addition, the SH-SB/Pt NPs had good catalytic activity between 20°C and 60°C as shown in **Figure 4b**. The catalytic activity of SH-SB/Pt NPs was the highest at 30°C. The catalytic activity of SH-SB/Pt NPs decreased gradually when the temperature was greater than 60°C, which should be

attributed to the rapid acceleration of the decomposition rate of H_2O_2 at this temperature. In short, the optimum reaction conditions for SH-SB/Pt NPs were pH 4 and 30°C.

In general, natural enzymes easily lose activity under high temperatures and harsh conditions such as excessive acid and alkali. The catalytic activity of SH-SB/Pt NPs was checked at different temperatures (20-70°C), pH (2-8), NaCl concentrations (0.2-5 mg/mL), storage time to evaluate the stability of SH-SB/Pt NPs. As shown in **Figure 4c**, the relative catalytic activity of SH-SB/Pt NPs remained higher than 86.61±2.56% after incubation with HAc-NaAc solution (pH 2-8) for 120 min. As shown in **Figure 4d**, the relative catalytic activity of SH-SB/Pt NPs remained higher than 81.65±1.70% after incubated at 20-70°C for 240 min. As shown in **Figure 4e**, SH-SB/Pt NPs maintained high relative activity (≥81±0.76%) in low concentration NaCl solution (0.2-5 mg/mL). As shown in **Figure 4f**, SH-SB/Pt NPs remained good catalytic activity (≥84.86±1.10%) in 1-30 d. In short, SH-SB/Pt NPs had good stability in different conditions, which should be due to the zwitterionic SH-SB layer that played a good stabilizing role on SH-SB/Pt NPs.

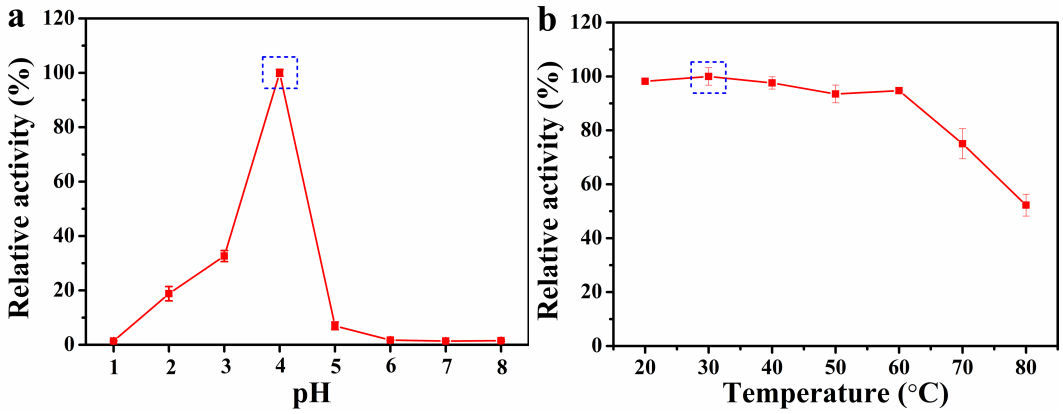

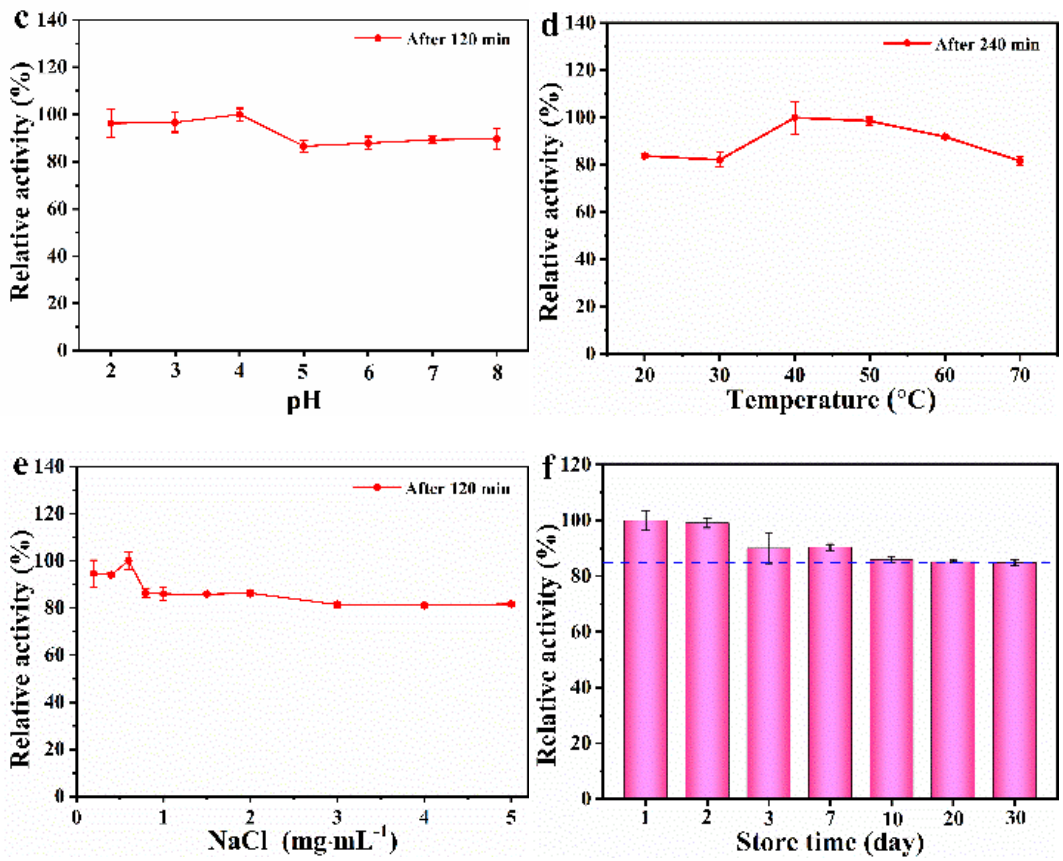

Figure 4. Optimum conditions for peroxidase activity of SH-SB/Pt NPs: (a) different pH (1-8); (b) different temperatures (20-80℃) and stability of SH-SB/Pt NPs under different conditions: (c) pH (2-8); (d) temperature (20-70℃); (e) NaCl concentration (0.2-5 mg/mL) and (f) storage time

3.5 Catalytic kinetics

The catalytic kinetics of SH-SB/Pt NPs was further studied by oxidation of TMB with H_2O_2. **Figure 5a** and **b** are Michaelis-Menten equations of TMB and H_2O_2, respectively. **Figure 5c** and **d** show a linear relationship between the reciprocal of the initial velocity (1/ *v*) and the reciprocal of the substrate concentration (1/*[S]*: $1/c_{TMB}$ or $1/c_{H2O2}$). According to Michaelis-Menten equation, the K_m values of TMB and H_2O_2 were 0.366 mM and 6.66 mM, respectively. The V_m values of TMB and H_2O_2 were 75.4×10^{-8} Ms^{-1} and 119.8×10^{-8} Ms^{-1}, respectively. The

K_m and V_m values of SH-SB/Pt NPs, HRP and other reported materials were summarized in **Table 1**. The K_m value is defined as the binding ability of the enzyme to substrate. Compared with HRP, the K_m value of substrate TMB (0.366 mM) of this work was lower than that of HRP (0.434 mM), indicating that the binding ability of SH-SB/Pt NPs to TMB was higher than that of HRP. The surface charge and chemical group of SH-SB/Pt NPs may facilitate the binding of substrate TMB. The V_m value of TMB of SH-SB/Pt NPs (75.40×10^{-8} Ms^{-1}) was 7.5 times than that of HRP (10.0×10^{-8} Ms^{-1}), indicating that SH-SB/Pt NPs had good catalytic capacity.

Table 1 Comparison of different catalytic kinetic parameters

Catalysts	K_m (mM)		V_m (10^{-8} Ms^{-1})		References
	TMB	H_2O_2	TMB	H_2O_2	
SH-SB/Pt NPs	0.377	6.660	75.40	119.8	this work
HRP	0.434	3.700	10.00	8.710	35
Au/Cu_2O	0.210	10.56	6.080	6.680	36
Pt/$CoFe_2O_4$	0.160	0.990	16.23	1.190	37
Cu-MOF	4.110	6.410	55.56	10.20	38
ZIF-67	13.69	19.90	31.96	1.920	39
MoS_2-$Pt_{74}Ag_{26}$	25.71	0.386	7.290	3.220	40

3.6 Detection of DA

SH-SB/Pt NPs can be used as a sensitive biosensor to detect DA due to the good peroxidase activity. In group [TMB+H_2O_2+SH-SB/Pt NPs], DA as a reducing agent easily undergoes redox reaction, leading to the inhibited oxidation of TMB. As the concentration of DA (0-220 μM)

gradually increased, the absorbance of the mixed solution at 652 nm gradually decreased in **Figure 5e**, the blue solution gradually faded in **Figure 5f**. Moreover, when the concentration of DA was in the range of 0-120 μM, ΔA ($\Delta A=A_{blank}-A_{DA}$) had a linear relationship with C_{DA}. The standard curve equation of DA was established ($y=0.00682C_{DA}-0.0587$, $R^2=0.993$), the limit of detection (LOD) was 0.244 μM. Compared with the reported biosensors in **Table 2**, colorimetric DA detection method established by SH-SB/Pt NPs had higher accuracy and wider detection range.

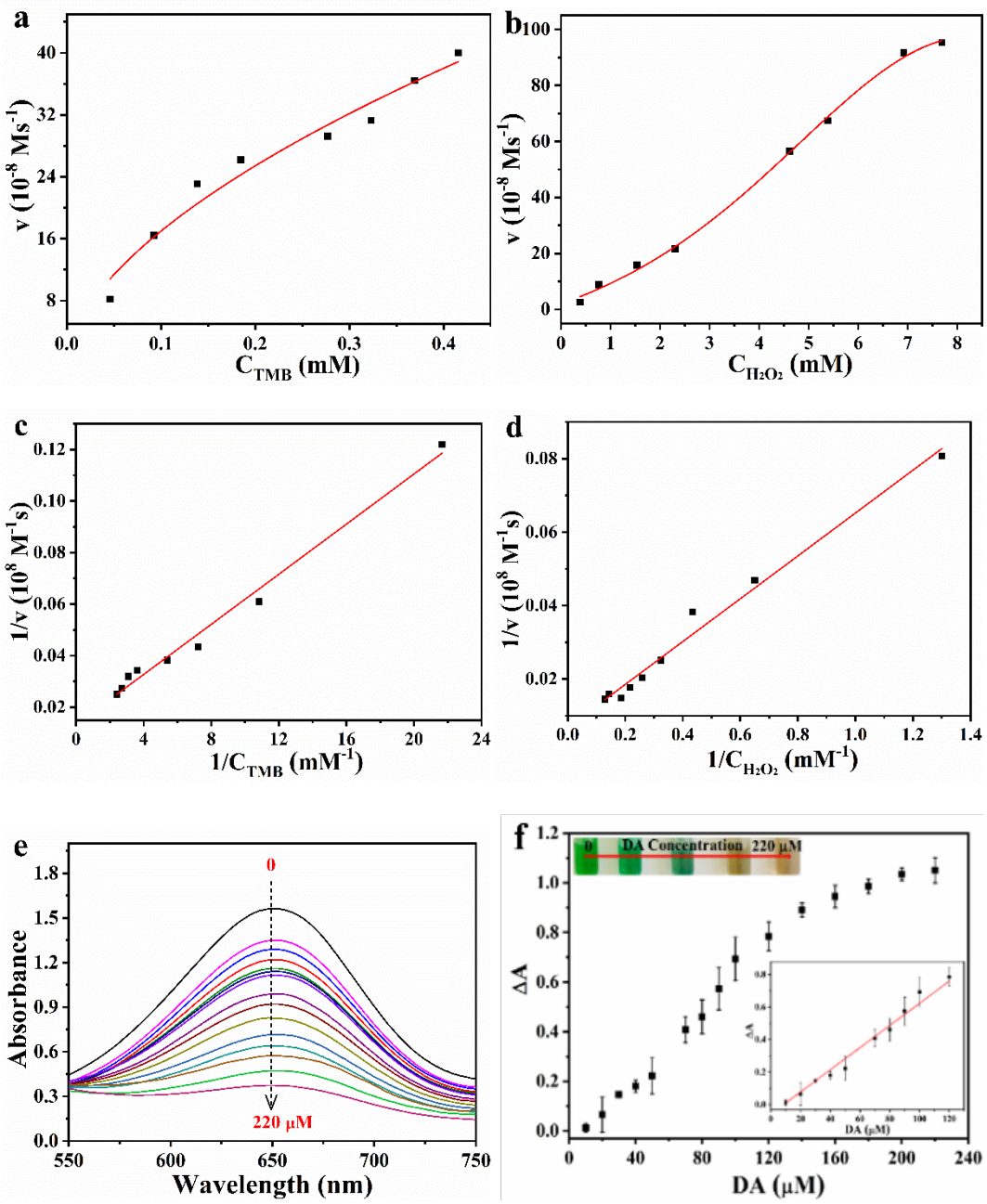

Figure 5. Catalytic kinetics of SH-SB/Pt NPs: (a) the TMB concentration: 0.046-0.415 mM (C_{H2O2}=50 mM); (b) the H_2O_2 concentration: 0.38-7.69 mM (C_{TMB}= 0.6 mM); (c) and (d) double reciprocal fitting diagram of initial reaction rate and substrate concentration; (e) and (f) establishment of DA test standard curve (0-220 μM)

Table 2 Comparison of detection range and LOD between SH-SB/Pt NPs and other nanomaterials

Nanomaterials	Detection method	Detection range (μM)	LOD (μM)	References
SH-SB/Pt NPs	Colorimetry	10-120	0.244	this work
Pt/$CoFe_2O_4$	Colorimetry	20-80	0.42	37
Pt/hBNNSs-5	Colorimetry	2-55	0.76	41
CuS-rGO	Colorimetry	2-100	0.47	42
h-CuS NCs	Colorimetry	2-150	1.67	43
rGO-Co_3O_4	Electrochemistry	0-30	0.389	44
HNP-PtTi	Electrochemistry	4-500	3.2	45
N-doped GQDs	Fluorometry	3-7	0.611	46
WS_2 QDs	Fluorometry	3-50	3.3	47

Table 3 Recovery rates of dopamine detected by SH-SB/Pt NPs in real samples

Sample	Real samples (mM)	Added DA (mM)	Final concentration (mM)	Recovery (%)	RSD (%)
DA solution 1	22.76±0.31	5	25.1±0.31	110.57	1.24
DA solution 2	11.83±0.83	20	29.28±1.04	108.71	2.83

The interfering substances exist in serum may affect the accuracy of detecting DA. we tested the selectivity of SH-SB/Pt NPs for DA detection. L-phenylalanine, L-tyrosine, L-lysine, L-histidine, Na^+, K^+, glucose, fructose and maltose were used to replace DA, and the concentration was 1200 μM. The ΔA of interfering substances was much smaller than that of DA (0.784±0.058), which proved that the biosensor based on SH-SB/Pt NPs had good selectivity. Based on the accuracy and selectivity of SH-SB/Pt NPs, the recovery rate of DA in real samples was studied. According to the DA standard curve equation, the recovery rate of

DA was 108.71-110.57% (**Table 3**). In summary, the new colorimetric sensor based on SH-SB/Pt NPs had high reliability and accuracy.

3.7 *In vitro* studies

In order to determine the anti-tumor ability of SH-SB/Pt NPs, we tested the photothermal properties. **Figure 6a** shows the temperature rise of SH-SB/Pt NPs, SH-SB, and K_2PtCl_4. Under the same initial temperature condition, the temperature of SH-SB/Pt NPs (C_{Pt}=0.336 mg/mL) rose from 27°C to 61.2°C within 1200 s. SH-SB/Pt NPs displayed the highest temperature in all samples. SH-SB/Pt NPs were stable after irradiation compared with the precipitated Pt NPs, which further proved that the modification of Pt NPs by SH-SB improved their temperature rise ability and stability. The different concentrations of SH-SB/Pt NPs were compared. **Figure 6b** shows that as the concentration of SH-SB/Pt NPs increased, the change of temperature increased. The temperature of SH-SB/Pt NPs rose to nearly 48°C even when the concentration of SH-SB/Pt NPs was 0.084 mg/mL. And we tested the temperature rising cycle curve of SH-SB/Pt NPs as shown in **Figure 6c**, which suggested that their excellent photothermal conversion efficiency was η=30.25%. **Figure 6d** shows the repeated thermal cycle of SH-SB/Pt NPs with 5 times. The data of the sixth cycle was not obviously different from the first cycle, which proved that SH-SB/Pt NPs had excellent stability in photothermal conversion. In summary, the modification of Pt NPs by SH-SB enhanced photothermal performance and photothermal stability of Pt NPs. The excellent photothermal conversion performance and good stability of SH-SB/Pt NPs would have great potential application in PTT of tumors.

The stability of SH-SB /Pt NPs in proteins was tested by the changes of hydrodynamic size before and after incubation with fibrinogen. As shown in **Figure 6e,** fibrinogen and SH-SB/Pt NPs were separately dissolved in PBS solution at pH7.4 and incubated for 24 h, the hydrodynamic size of fibrinogen and SH-SB/Pt NPs were 22.28 nm and 17.02 nm, respectively. Then fibrinogen, SH-SB /Pt NPs were mixed and co-incubated for 24 h, the hydrodynamic size of the mixed solution was 19.58 nm, which was between fibrinogen and SH-SB/Pt NPs. The results demonstrated that SH-SB/Pt NPs did not cause the aggregation of fibrinogen, which proved that SH-SB/Pt NPs had good stability. This may be due to the strong hydrophilicity of SH-SB with zwitterionic groups, which resulted from low protein adsorption of SH-SB. Furthermore, the blood of mice was taken for a hemolysis test to investigate whether SH-SB/Pt NPs could cause hemolysis. As shown in **Figure 6f**, with the increase of SH-SB/Pt NPs concentration from 12.5 to 1600 μg/mL, the hemolysis rate remained below 5%, which proved that SH-SB/Pt NPs did not cause obvious hemolysis in mice, indicating that SH-SB/Pt NPs had excellent biocompatibility towards RBCs.

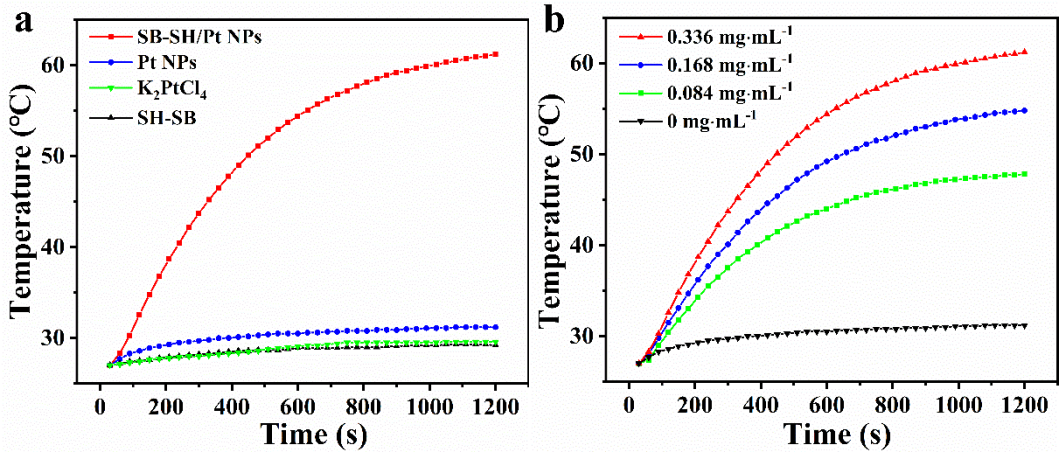

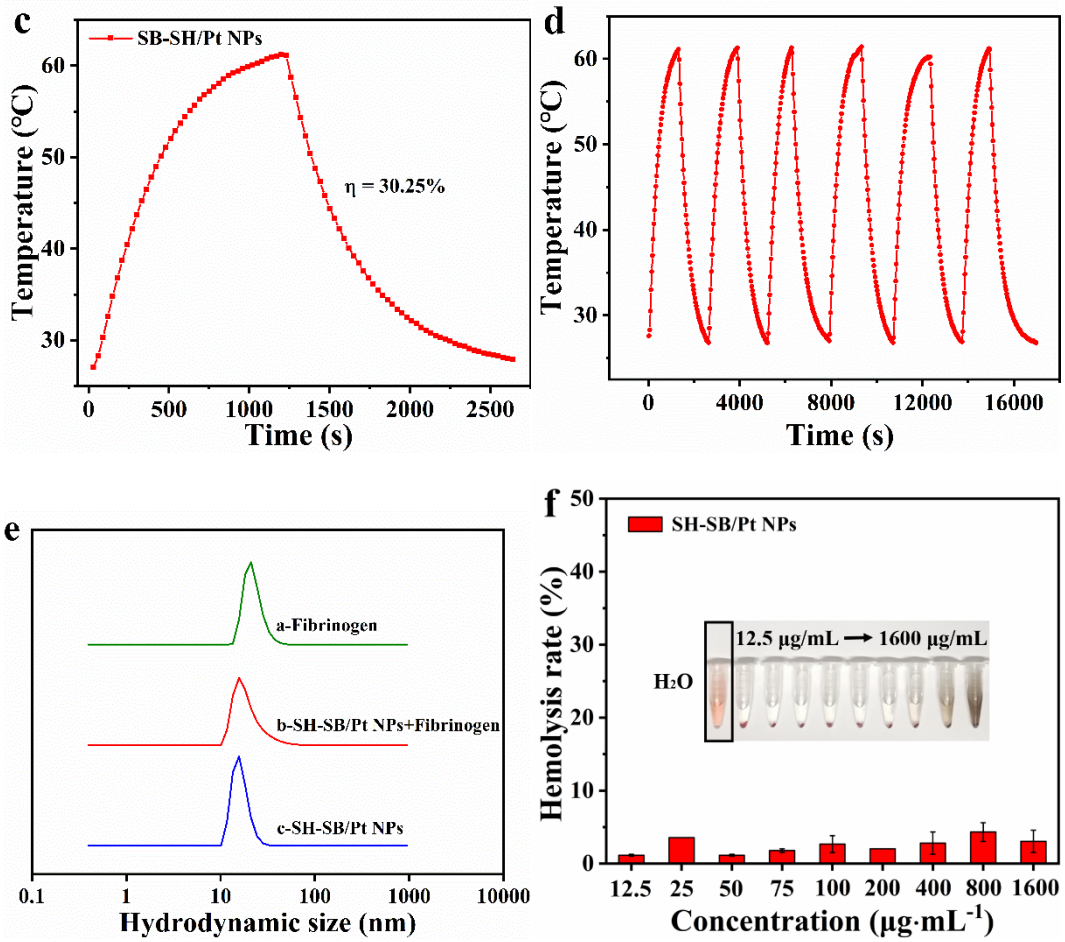

Figure 6. Thermal performance of SH-SB/Pt NPs: (a) photothermal properties of SH-SB/Pt NPs, Pt NPs, K_2PtCl_4 and SH-SB in 1200 s, (b) photothermal properties of SH-SB/Pt NPs at different concentrations in 1200 s, (c) single and (d) multiple temperature rise cycle curves for SH-SB/Pt NPs (C_{Pt}=0.336 mg·mL^{-1}); (e) the stability of SH-SB/Pt NPs in protein solution; (f) hemolysis rate of different concentration of SH-SB/Pt NPs

HeLa and A549 cells were used to study the tumor suppressive ability of SH-SB/Pt NPs by MTT assay *in vitro*. **Figure 7a** and **b** illustrated the viability of cells treated with SH-SB, Pt NPs and SH-SB/Pt NPs at the same concentration. SH-SB and Pt NPs had little effect on the proliferation of the two kinds of cells. In contrast, the cell viability of SH-SB /Pt NPs was lower

than that of SH-SB and Pt NPs, which may be because the stable SH-SB/Pt NPs with small size had strong catalytic ability. More importantly, the viabilities of SH-SB/Pt NPs+NIR (C_{Pt}=100 μg/mL) treated with HeLa cells and A549 cells were low to 40% and 20%, respectively, which should be attributed to the good photothermal conversion performance and catalytic capacity of SH-SB/Pt NPs. Furthermore, the effect of NIR laser on the tumor suppressive ability of SH-SB/Pt NPs was studied. **Figure 7c** and **d** show that with the increase of the concentration of SH-SB/Pt NPs, the tumor suppressive ability gradually increased. With the addition of NIR laser, the tumor suppressive ability of SH-SB/Pt NPs was further enhanced. When the concentration of SH-SB/Pt NPs was 200 μg/mL, the viability of tumor cells with laser irradiation was low to about 10%.

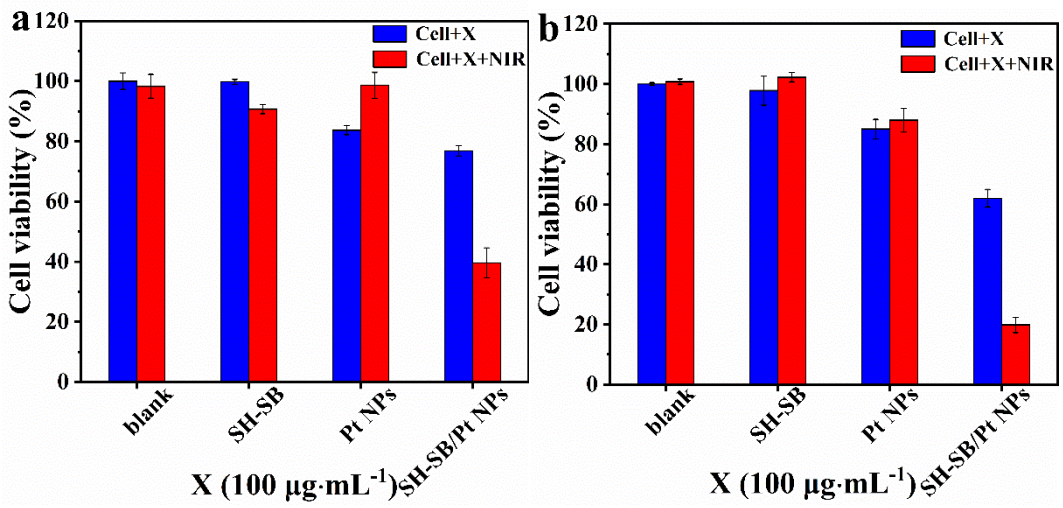

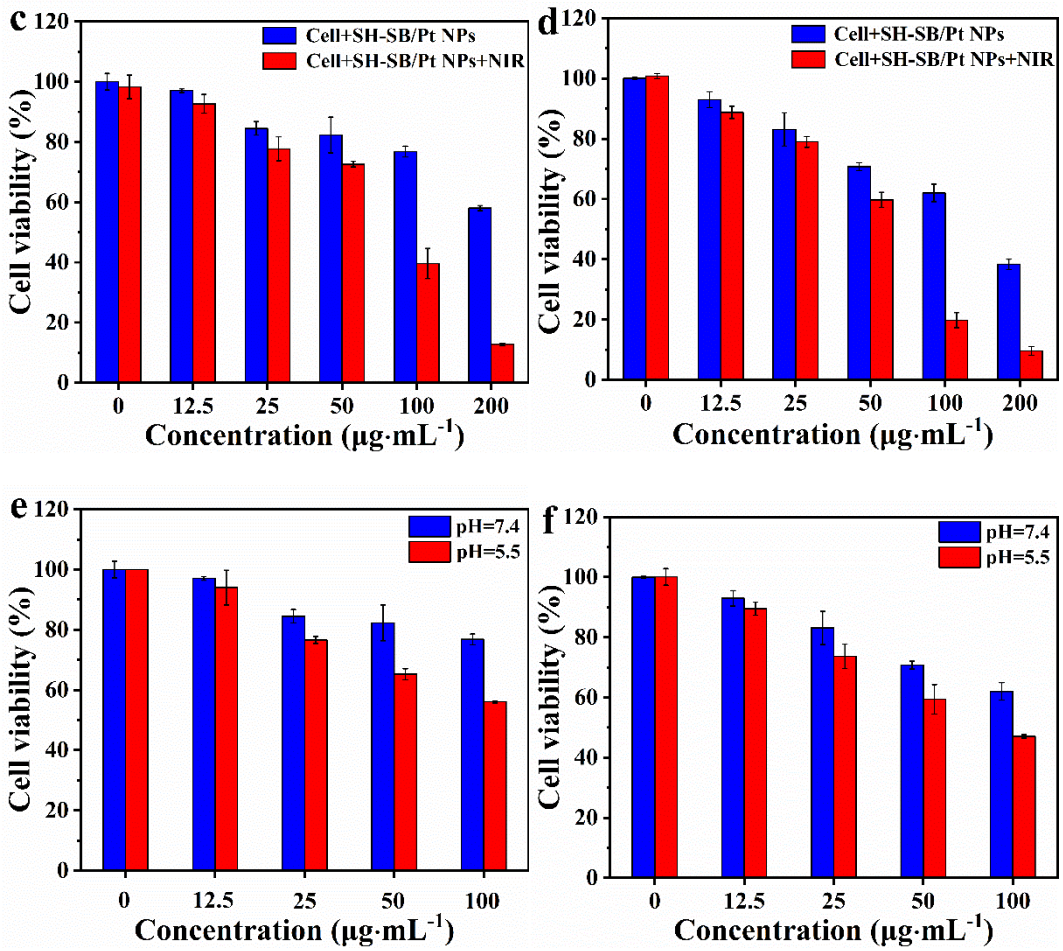

Figure 7. Cytotoxicity of SH-SB/Pt NPs and NIR co-treatment of HeLa cells and A549 cells. (a) HeLa cells and (b) A549 cells treated with 100 μg/mL of different samples, the toxicity of different concentrations of SH-SB/Pt NPs to (c)HeLa cells and (d) A549 cells, the toxicity of SH-SB/Pt NPs to (e) HeLa cells and (f) A549 cells at different pH.

In addition, we simulated the acidic environment of the tumor to further investigate whether the tumor suppressive ability of SH-SB/Pt NPs was affected. As shown in **Figure 7e** and **f**, the cell viability with environmental pH 5.5 was lower than pH 7.4 after the addition of SH-SB/Pt NPs, which was because SH-SB/Pt NPs had catalytic activity at slightly acidic conditions. SH-SB/Pt NPs were more likely to catalyze endogenous O_2 and H_2O_2 to produce more ROS when

the pH was closer to the optimal pH 4. SH-SB/Pt NPs and NIR co-treatment had strong destruction or inhibition effect on acidic tumor cells, and also laid a solid foundation for subsequent tumor suppression experiments *in vivo*. Therefore, SH-SB/Pt NPs can be used to treat cancer in combination with PTT and CDT.

3.8 Anti-tumor effect *in vivo*

Based on the photothermal properties of SH-SB/Pt NPs and the results of cell viability *in vitro*, the tumor inhibition performance of SH-SB/Pt NPs was studied *in vivo*. The initial body weight of each group was similar, and the trend of body weight change of experimental groups was the same as Saline group as shown in **Figure 8a**. The effect of SH-SB/Pt NPs on the weight of mice was relatively small. The viscera indexes of treated and blank mice were similar as shown in **Figure 8b**. As depicted in **Figure S4a**, organs of all groups were almost the same size. Thus, the injection of SH-SB/Pt NPs did not cause obvious organ damage in mice, proving the biocompatibility of SH-SB/Pt NPs. In order to further reveal whether SH-SB/Pt NPs has damage to liver function, the serum of mice was detected by AST/ALT to obtain the liver function indexes. As shown in **Figure 8c**, AST and ALT indexes of the SH-SB/Pt NPs+NIR group were 81.76% and 110.24% compared with Saline group, which proved that SH-SB/Pt NPs-assisted PTT had no effect on the liver function basically, further reflecting the biological safety of SH-SB/Pt NPs+NIR.

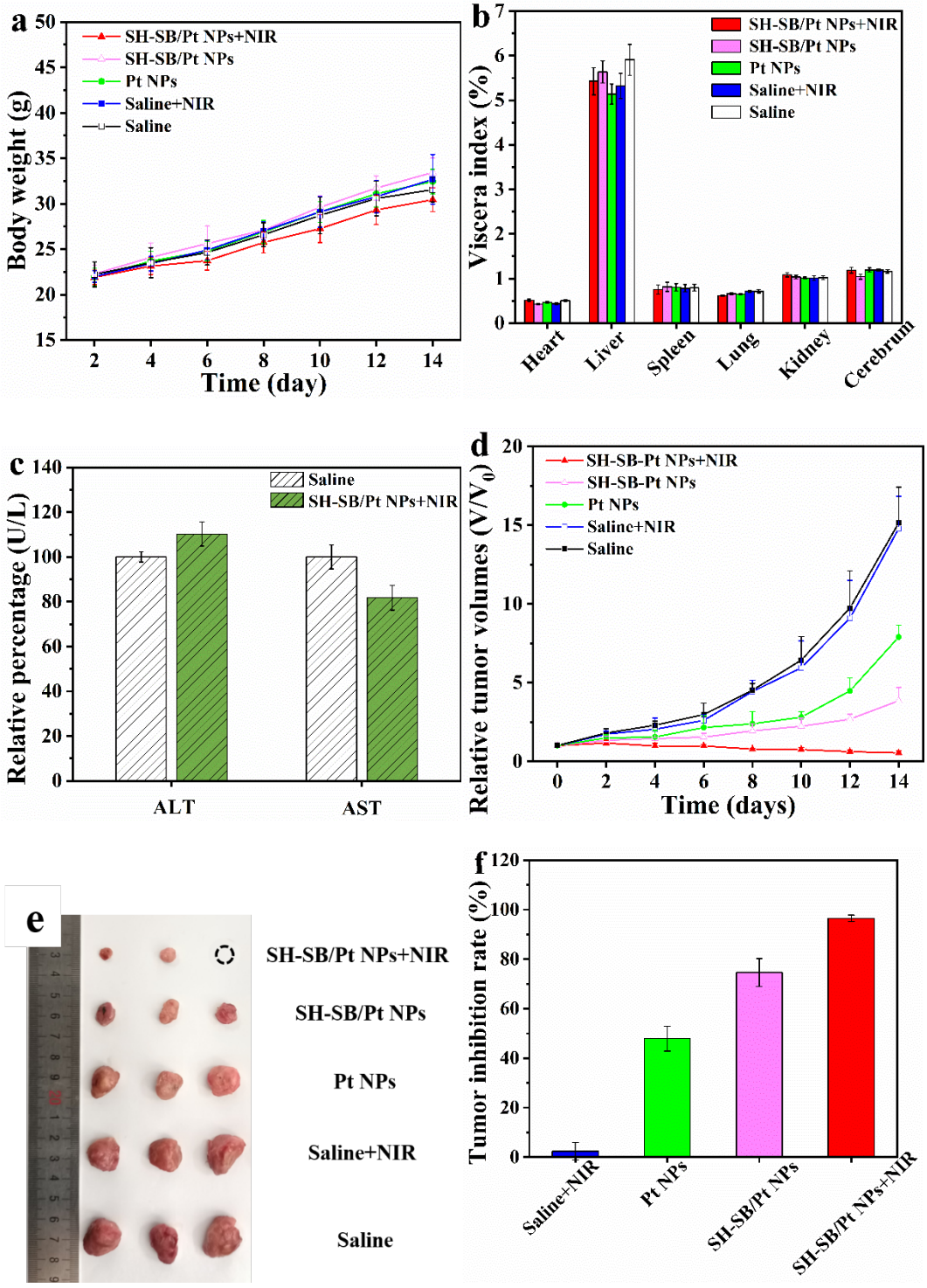

Figure 8. (a) Body weight, (b) visceral index of treated mice, (c) AST and ALT of mice after 14 days of treatment and (d) relative tumor volumes, (e) tumor image of groups and (f) tumor inhibition rate

The long diameter and short diameter of tumor were measured to calculate the relative tumor volume and tumor inhibition rate of each group. **Figure S4b** is the image of mice on the 14th day, the mice had a tumor on the right hip. As shown in **Figure 8d** and **(e)**, SH-SB/Pt NPs+NIR group had the best anti-tumor effect *in vivo* after 14 days of treatment. The relative tumor volume of the Saline group and the Saline +NIR group increased to 15.15±2.27 and 14.79±2.05, and the tumor inhibition rate of the Saline +NIR group was 2.38±3.55%. On the contrary, the relative tumor volume of SH-SB/Pt NPs was 3.84±0.85, which was significantly lower than that of Pt NPs (7.89±0.76). The SH-SB/Pt NPs+NIR group (0.53±0.13) was much lower than other groups. The tumor inhibition rate of SH-SB/Pt NPs+NIR was 96.48±1.32%, which was the highest in all groups in **Figure 8f**. This demonstrated that SH-SB/Pt NPs successfully suppressed the proliferation of tumor cells by photothermal ability and CDT *in vivo*, protecting normal organisms from suffering from cancer.

4. CONCLUSION

In summary, we prepared Pt-based nanozymes with different ligands, namely SH-SB/Pt NPs, β-MEA/Pt NPs and 3-MPA/Pt NPs, and revealed the effect of surface ligand on their zeta potential and catalytic activity. In addition, the catalytic activities of the three nanoparticles were compared under the same conditions, and the optimum conditions for TMB catalyzed by SH-SB/Pt NPs were determined. SH-SB/Pt NPs stabilized by zwitterionic SH-SB had the most homogeneous dispersion, best stability and highest catalytic activity in solution. The optimal conditions for SH-SB/Pt NPs to catalyze TMB were pH 4 and 30°C. A colorimetric bioassay

platform for DA was established with a wide range (0-120 μM), low detection limit (0.244 μM), and high specificity based on the peroxidase property of SH-SB/Pt NPs. Finally, SH-SB/Pt NPs displayed high photothermal conversion efficacy and stability. Besides, tumor suppression experiments *in vitro* and *in vivo* were performed based on SH-SB/Pt NPs, which demonstrated that SH-SB/Pt NPs inhibited cancer cells and tumors through PTT and CDT. Therefore, the study of SH-SB/Pt NPs nanozymes revealed the catalytic activity of nanozymes can be tuned by controlling the surface ligands, which will have great application in the field of catalysis and biomedicine for tumor treatment.

ASSOCIATED CONTENT

Part of experimental section; UV-Vis of SH-SB/Pt NPs, β-MEA/Pt NPs and 3-MPA/Pt NPs; EDX, XPS, SEM mapping and FTIR of SH-SB/Pt NPs and images of viscera and mice after 14 days of treatment (PDF)

AUTHOR INFORMATION

Corresponding Author

Longgang Wang - State Key Laboratory of Metastable Materials Science and Technology, Hebei Key Laboratory of Nano-biotechnology, Hebei Key Laboratory of Applied Chemistry, Yanshan University, Qinhuangdao, 066004, China

Phone: + (86) 18330368290; Email: lgwang@ysu.edu.cn

Author Contributions

Ruyu Li: Investigation, Writing - Original Draft Liyuan Fan: Investigation Shengfu Chen: Writing-Reviewing and Editing Longgang Wang: Supervision, Writing - Review & Editing Yanshuai Cui: Conceptualization, Writing - Review & Editing Guanglong Ma: Writing-Reviewing and Editing Xiaoyu Zhang: Methodology Zhiwei Liu: Methodology

Notes

The authors declare no competing financial interest.

ACKNOWLEDGMENT

The authors appreciate financial support from Science and Technology Project of Hebei Education Department (QN2022124), Natural Science Foundation of Hebei Province (B2017203229, H2022203004), Subsidy for Hebei Key Laboratory of Applied Chemistry after Operation Performance (22567616H), Key Program of Hebei University of Environmental Engineering (2020ZRZD02), and Science and Technology Support Program of Qinhuangdao (202101A007, 201902A191), National Nature Science Foundation of China (21674092, 21975216 and 21474085), The Zhejiang Provincial Natural Science Foundation of China (LZ20B040001).

ABBREVIATIONS

SH-SB, Sulfhydryl sulfobetaine; β-MEA ， β-mercaptoethylamine; 3-MPA, 3-mercaptopropionic acid; DA, dopamine; SH-SB/Pt NPs, SH-SB modified platinum nanoparticles; β-MEA/Pt NPs, β-MEA modified platinum nanoparticles; 3-MPA/Pt NPs, 3-MPA modified platinum nanoparticles.

REFERENCES

(1) Tao, Y.; Vermilyea, S. C.; Zammit, M.; Lu, J.; Olsen, M.; Metzger, J. M.; Yao, L.; Chen, Y.; Phillips, S.; Holden, J. E.; et al. Autologous transplant therapy alleviates motor and depressive behaviors in parkinsonian monkeys. *Nat Med* **2021**, *27* (4), 632-639.

(2) Schmack, K.; Bosc, M.; Ott, T.; Sturgill, J. F.; Kepecs, A. Striatal dopamine mediates hallucination-like perception in mice. *Science* **2021**, *372* (6537), eabf4740.

(3) Cai, Y.; Nielsen, B. E.; Boxer, E. E.; Aoto, J.; Ford, C. P. Loss of nigral excitation of cholinergic interneurons contributes to parkinsonian motor impairments. *Neuron* **2021**, *109* (7), 1137-1149 e1135.

(4) Mao, Y.; Gao, S.; Yao, L.; Wang, L.; Qu, H.; Wu, Y.; Chen, Y.; Zheng, L. Single-atom nanozyme enabled fast and highly sensitive colorimetric detection of Cr(VI). *J Hazard Mater* **2021**, *408*, 124898.

(5) Wang, X.; Liao, X.; Mei, L.; Zhang, M.; Chen, S.; Qiao, X.; Hong, C. An immunosensor using functionalized Cu_2O/Pt NPs as the signal probe for rapid and highly sensitive CEA detection with colorimetry and electrochemistry dual modes. *Sens. Actuators, B* **2021**, *341*, 130032.

(6) Martell, J. D.; Yamagata, M.; Deerinck, T. J.; Phan, S.; Kwa, C. G.; Ellisman, M. H.; Sanes, J. R.; Ting, A. Y. A split horseradish peroxidase for the detection of intercellular protein–protein interactions and sensitive visualization of synapses. *Nat. Biotechnol* **2016**, *34* (7), 774-780.

(7) Yu, Z.; Zhou, P.; Pan, W.; Li, N.; Tang, B. A biomimetic nanoreactor for synergistic chemiexcited photodynamic therapy and starvation therapy against tumor metastasis. *Nat. Commun* **2018**, *9* (1), 5044.

(8) Li, J.; Wu, Y.; Qin, Y.; Liu, M.; Chen, G.; Hu, L.; Gu, W.; Zhu, C. AgCu@CuO aerogels with peroxidase-like activities and photoelectric responses for sensitive biosensing. *Chem Commun (Camb)* **2021**, *57* (100), 13788-13791.

(9) Gao, L.; Zhuang, J.; Nie, L.; Zhang, J.; Zhang, Y.; Gu, N.; Wang, T.; Feng, J.; Yang, D.; Perrett, S.; et al. Intrinsic peroxidase-like activity of ferromagnetic nanoparticles. *Nat. Nanotechnol* **2007**, *2* (9), 577-583.

(10) Wang, H.; Wan, K.; Shi, X. Recent advances in nanozyme research. *Adv. Mater* **2019**, *31* (45), 1805368.

(11) Gu, H.; Huang, Q.; Zhang, J.; Li, W.; Fu, Y. Heparin as a bifunctional biotemplate for Pt nanocluster with exclusively peroxidase mimicking activity at near-neutral pH. *Colloid. Surface. A* **2020**, *606*, 125455.

(12) Meng, X.; Li, D.; Chen, L.; He, H.; Wang, Q.; Hong, C.; He, J.; Gao, X.; Yang, Y.; Jiang, B.; et al. High-performance self-cascade pyrite nanozymes for apoptosis-ferroptosis synergistic tumor therapy. *Acs Nano* **2021**, *15* (3), 5735-5751.

(13) Fan, K.; Xi, J.; Fan, L.; Wang, P.; Zhu, C.; Tang, Y.; Xu, X.; Liang, M.; Jiang, B.; Yan, X.; et al. In vivo guiding nitrogen-doped carbon nanozyme for tumor catalytic therapy. *Nat. Commun.* **2018**, *9*, 1440.

(14) Chang, B.; Zhang, L.; Wu, S.; Sun, Z.; Cheng, Z. Engineering single-atom catalysts toward biomedical applications. *Chem. Soc. Rev* **2022**, *51* (9), 3688-3734.

(15) Wang, L.; Gao, F.; Wang, A.; Chen, X.; Li, H.; Zhang, X.; Zheng, H.; Ji, R.; Li, B.; Yu, X.; et al. Defect-rich adhesive molybdenum disulfide/rGO vertical heterostructures with enhanced nanozyme activity for smart bacterial killing application. *Adv. Mater* **2020**, *32* (48), 2005423.

(16) Liu, T.; Li, Z.; Chen, M.; Zhao, H.; Zheng, Z.; Cui, L.; Zhang, X. Sensitive electrochemical biosensor for Uracil-DNA glycosylase detection based on self-linkable hollow Mn/Ni layered doubled hydroxides as oxidase-like nanozyme for cascade signal amplification. *Biosens Bioelectron* **2021**, *194*, 113607.

(17) Liu, W.; Chu, L.; Zhang, C.; Ni, P.; Jiang, Y.; Wang, B.; Lu, Y.; Chen, C. Hemin-assisted synthesis of peroxidase-like Fe-N-C nanozymes for detection of ascorbic acid-generating bio-enzymes. *Chem. Eng. J* **2021**, *415*, 128876.

(18) Jeon, S. W.; Song, I.; Lee, H.; Kim, J.; Byun, Y.; Koh, D. J.; Kim, D. H. Enhanced SO_2 resistance of V_2O_5/WO_3-TiO_2 catalyst physically mixed with alumina for the selective catalytic reduction of NO_x with NH_3. *Chem. Eng. J* **2022**, *433*, 133836.

(19) Li, S.; Tian, W.; Liu, Y. The ligand effect of atomically precise gold nanoclusters in tailoring catalytic properties. *Nanoscale* **2021**, *13* (40), 16847-16859.

(20) Liu, Y.; Qin, Y.; Zhang, Q.; Zou, W.; Jin, L.; Guo, R. Arginine-rich peptide/platinum hybrid colloid nanoparticle cluster: A single nanozyme mimicking multi-enzymatic cascade systems in peroxisome. *J Colloid Interface Sci* **2021**, *600*, 37-48.

(21) Deng, H.; Zhang, J.; Yang, Y.; Yang, J.; Wei, Y.; Ma, S.; Shen, Q. Chemodynamic and photothermal combination therapy based on dual-modified metal-organic framework for inducing tumor ferroptosis/pyroptosis. *ACS Appl Mater Interfaces* 2022, *14* (21), 24089-24101.

(22) He, J.; Yu, S.; Ma, Z.; Sun, H.; Yang, Q.; Liu, Z.; Wang, X.; Zhang, X.; Wang, L. Polymyxin E biomineralized and doxorubicin-loaded gold nanoflowers nanodrug for chemo-photothermal therapy. *Int. J. Pharm* **2022**, *625*, 122082.

(23) Zhang, J.; Huang, Z.; Xie, Y.; Jiang, X. Modulating the catalytic activity of gold nanoparticles using amine-terminated ligands. *Chem. Sci* **2022**, *13* (4), 1080-1087.

(24) Yang, Q.; Li, L.; Sun, L.; Ye, Z.; Wang, Y.; Guo, X. Spherical polyelectrolyte brushes as bio-platforms to integrate platinum nanozyme and glucose oxidase for colorimetric detection of glucose. *J. Polym Sci* **2021**, *59* (19), 2201-2211.

(25) Li, J.; Liu, W.; Wu, X.; Gao, X. Mechanism of pH-switchable peroxidase and catalase-like activities of gold, silver, platinum and palladium. *Biomaterials* **2015**, *48*, 37-44.

(26) Yang, K.; Yue, L.; Yu, G.; Rao, L.; Tian, R.; Wei, J.; Yang, Z.; Sun, C.; Zhang, X.; Xu, M.; et al. A hypoxia responsive nanoassembly for tumor specific oxygenation and enhanced sonodynamic therapy. *Biomaterials* **2021**, *275*, 120822.

(27) Fu, S.; Yang, R.; Zhang, L.; Liu, W.; Du, G.; Cao, Y.; Xu, Z.; Cui, H.; Kang, Y.; Xue, P. Biomimetic CoO@AuPt nanozyme responsive to multiple tumor microenvironmental clues for augmenting chemodynamic therapy. *Biomaterials* **2020**, *257*, 120279.

(28) Chen, Z.; Chen, R.; Zhao, C.; Quan, Z.; Zhu, H.; Wang, L.; Bu, Q.; He, Y.; He, H. A novel medically imageable intelligent cellulose nanofibril-based injectable hydrogel for the chemo-photothermal therapy of tumors. *Chem. Eng. J* **2022**, *431*, 133255.

(29) Sun, H.; Chang, M. Y. Z.; Cheng, W.-I.; Wang, Q.; Commisso, A.; Capeling, M.; Wu, Y.; Cheng, C. Biodegradable zwitterionic sulfobetaine polymer and its conjugate with paclitaxel for sustained drug delivery. *Acta Biomater* **2017**, *64*, 290-300.

(30) Zhu, M.; Lu, J.; Hu, Y.; Liu, Y.; Hu, S.; Zhu, C. Photochemical reactions between 1,4-benzoquinone and O_2(*). *Environ Sci Pollut Res Int* **2020**, *27* (25), 31289-31299.

(31) Lyu, Z.; Xu, M.; Wang, J.; Li, A.; François-Xavier Corvini, P. Hierarchical nano-vesicles with bimetal-encapsulated for peroxymonosulfate activation: Singlet oxygen-dominated

oxidation process. *Chem. Eng. J* **2022**, *433*, 133581.

(32) Wang, P.; Li, X.; Fan, S.; Chen, X.; Qin, M.; Long, D.; Tadé, M. O.; Liu, S. Impact of oxygen vacancy occupancy on piezo-catalytic activity of $BaTiO_3$ nanobelt. *Appl. Catal., B* **2020**, *279*, 119340.

(33) Liu, X.; Yan, L.; Ren, H.; Cai, Y.; Liu, C.; Zeng, L.; Guo, J.; Liu, A. Facile synthesis of magnetic hierarchical flower-like Co_3O_4 spheres: Mechanism, excellent tetra-enzyme mimics and their colorimetric biosensing applications. *Biosens Bioelectron* **2020**, *165*, 112342.

(34) He, J.; Wang, J.; Gao, S.; Cui, Y.; Ji, X.; Zhang, X.; Wang, L. Biomineralized synthesis of palladium nanoflowers for photothermal treatment of cancer and wound healing. *Int. J. Pharm* **2022**, *615*, 121489.

(35) Dong, L.; Li, R.; Wang, L.; Lan, X.; Sun, H.; Zhao, Y.; Wang, L. Green synthesis of platinum nanoclusters using lentinan for sensitively colorimetric detection of glucose. *Int J Biol Macromol* **2021**, *172*, 289-298.

(36) Jiao, A.; Xu, L.; Tian, Y.; Cui, Q.; Liu, X.; Chen, M. Cu_2O nanocubes-grafted highly dense Au nanoparticles with modulated electronic structures for improving peroxidase catalytic performances. *Talanta* **2021**, *225*, 121990.

(37) He, F.; Li, W.; Zhao, F.; Zhu, X.; Liu, Q.; Liu, Z.; Zhang, X.; Zhang, X. Pt deposited on magnetic $CoFe_2O_4$ nanoparticles: Double enzyme-like activity, catalytic mechanism and fast colorimetric sensing of dopamine. *Microchem. J* **2020**, *158*, 105264.

(38) Wang, C.; Gao, J.; Tan, H. Integrated Antibody with Catalytic Metal-organic framework for colorimetric immunoassay. *ACS Appl Mater Interfaces* **2018**, *10* (30), 25113-25120.

(39) Wang, S.; Xu, D.; Ma, L.; Qiu, J.; Wang, X.; Dong, Q.; Zhang, Q.; Pan, J.; Liu, Q. Ultrathin

ZIF-67 nanosheets as a colorimetric biosensing platform for peroxidase-like catalysis. *Anal Bioanal Chem* **2018**, *410* (27), 7145-7152.

(40) Cai, S.; Han, Q.; Qi, C.; Lian, Z.; Jia, X.; Yang, R.; Wang, C. $Pt_{74}Ag_{26}$ nanoparticle-decorated ultrathin MoS_2 nanosheets as novel peroxidase mimics for highly selective colorimetric detection of H_2O_2 and glucose. *Nanoscale* **2016**, *8* (6), 3685-3693.

(41) Ivanova, M. N.; Grayfer, E. D.; Plotnikova, E. E.; Kibis, L. S.; Darabdhara, G.; Boruah, P. K.; Das, M. R.; Fedorov, V. E. Pt-decorated boron nitride nanosheets as artificial nanozyme for detection of dopamine. *ACS Appl Mater Interfaces* **2019**, *11* (25), 22102-22112.

(42) Dutta, S.; Ray, C.; Mallick, S.; Sarkar, S.; Sahoo, R.; Negishi, Y.; Pal, T. A gel-based approach to design hierarchical CuS decorated reduced graphene oxide nanosheets for enhanced peroxidase-like activity leading to colorimetric detection of dopamine. *J. Phys. Chem. C* **2015**, *119* (41), 23790-23800.

(43) Zhu, J.; Peng, X.; Nie, W.; Wang, Y.; Gao, J.; Wen, W.; Selvaraj, J. N.; Zhang, X.; Wang, S. Hollow copper sulfide nanocubes as multifunctional nanozymes for colorimetric detection of dopamine and electrochemical detection of glucose. *Biosens Bioelectron* **2019**, *141*, 111450.

(44) Numan, A.; Shahid, M. M.; Omar, F. S.; Ramesh, K.; Ramesh, S. Facile fabrication of cobalt oxide nanograin-decorated reduced graphene oxide composite as ultrasensitive platform for dopamine detection. *Sens. Actuators, B* **2017**, *238*, 1043-1051.

(45) Zhao, D.; Yu, G.; Tian, K.; Xu, C. A highly sensitive and stable electrochemical sensor for simultaneous detection towards ascorbic acid, dopamine, and uric acid based on the hierarchical nanoporous PtTi alloy. *Biosens Bioelectron* **2016**, *82*, 119-126.

(46) Ma, Y.; Chen, A. Y.; Xie, X. F.; Wang, X. Y.; Wang, D.; Wang, P.; Li, H. J.; Yang, J. H.; Li,

Y. Doping effect and fluorescence quenching mechanism of N-doped graphene quantum dots in the detection of dopamine. *Talanta* **2019**, *196*, 563-571.

(47) Zhao, X.; He, D.; Wang, Y.; Fu, C. Facile fabrication of tungsten disulfide quantum dots (WS_2 QDs) as effective probes for fluorescence detection of dopamine (DA). *Mater. Chem. Phys* **2018**, *207*, 130-134.